

Stochastic additive manufacturing simulation: from experiment to surface roughness and porosity prediction

Yangfan Li^a, Ye Lu^{a,*}, Abdullah Al Amin^a, Wing Kam Liu^{a,*}

^a*Department of Mechanical Engineering, Northwestern University, Evanston, 60208, IL, USA*

Abstract

Deterministic computational modeling of laser powder bed fusion (LPBF) process fails to capture irregularities and roughness of the scan track, unless expensive powder-scale analysis is used. In this work we developed a stochastic computational modeling framework based on Markov Chain Monte Carlo (MCMC) capable of capturing the irregularities of LPBF scan. The model is calibrated against AFRL single track scan data using a specially designed tensor decomposition method, i.e., Higher-Order Proper Generalized Decomposition (HOPGD) that relies on non-intrusive data learning and construction of reduced order surrogate models. Once calibrated, the stochastic model can be used to predict the roughness and porosity at part scale at a significantly reduced computational cost compared to detailed powder-scale deterministic simulations. The stochastic simulation predictions are validated against AFRL multi-layer and multitrack experiments and reported as more accurate when compared with regular deterministic simulation results.

Keywords: Additive manufacturing, Surface roughness, Lack of fusion porosity, Uncertainty quantification and propagation

1. Introduction

Even though Laser powder bed fusion (L-PBF), a promising Additive Manufacturing (AM) process is widely used in the aerospace, automotive, and biomedical industries [1, 2, 3], the processing-structure-properties-performance (PSPP) relationship must be understood before the industry can rely upon AM to produce components with consistent mechanical properties for parts under fatigue loading. Fatigue failure, one of the most common damage modes in cyclically loaded metallic materials, is influenced by defects within components inherently created by laser powder bed fusion (L-PBF) Additive Manufacturing (AM) processes. AM inherently created defects such as surface roughness and porosity, which may occur due to improper melt pool formation from insufficient melting caused by too little energy absorption or trapped gas caused by vaporization [4, 5], are driving factors in the fatigue performance of AM

*Co-corresponding authors

Email addresses: ye.lu@northwestern.edu (Ye Lu), w-liu@northwestern.edu (Wing Kam Liu)

components [6]. To choose the optimal manufacturing workflow, one must understand the surface roughness capabilities of metal AM, as well as post-processing techniques and their associated time and cost. The reduction of porosity also reduces the risk of cracks and fatigue fractures. The surface roughness and porosity of a part is critical to its function and long-term performance [7]. However, the prediction of surface roughness and porosity generally requires detailed simulations and is time-consuming [8] and therefore rarely used for large component scale analysis. Thus, more efficient approaches should be introduced into AM simulation models to find the relations between computation inputs and the mechanical performance of AM-built parts.

The formation of a melt pool, which is an intermediate step between solidification and laser source absorption, plays an important role in the description of interactions between powder materials [9]. In L-PBF, the localized solid powder is heated up and melted into a liquid after absorbing energy from the passing laser, then cools down and solidifies into a bulk material with a resultant microstructure as the laser moves further away. The melt pool acts as an effective index for the overall product quality since its geometrical characteristics, as one of the most important process signatures developed during an AM process [10], have huge influence on various properties of AM parts. A good predictive capability for the melt pool geometry can help on an efficient control of surface roughness. Besides, the melt pool cross-sectional area, which is typically measured by the pool width and depth, largely determines the porosity formation due to insufficient pool overlapping [11]. Thus, the computational model that manipulates process parameters such as laser power, scan speed, and spot size can be built to control the melt pool as well as the corresponding mechanical behaviors [12].

Computational models have been widely used in additive manufacturing due to their high flexibility and efficiency, and many efforts on understanding the influence of process parameters on part quality are made. Finite element/volume method-based thermal model, which defines as a highly transient manufacturing process, is one of the most popular means. For example, a finite-volume-based simulation model is built by Ghosh et al. and is validated through experimental melt pool geometries with multiple laser power and scan speed combinations [13]. A thermodynamically consistent model is also proposed for microstructure evolution during AM process using finite element method [14]. However, the lack of consideration on fluid flow in the melt pool neglects the effects of cooling through fluid convection, and makes the above models less accurate than thermal-fluid flow models when predicting the melt pool geometries [15]. Among different thermal fluid models, Gan et al. proposed a well-tested transient three-dimensional thermal-fluid computational model to predict the thermal field in the entire part and velocity field in the melt pool region [12]. The model is calibrated through highly controlled experiments made by Additive Manufacturing (AM) Modeling Challenge Series in 2020 [16] to validate and ensure the accuracy. Although the above model has accurately predicted melt pool geometries, the lack of stochastic information limits its capacity for predicting parts surface defects (e.g., surface roughness [17]) and volumetric structural defects (e.g., porosity [18]).

The defects in AM product quality are mostly caused by uncertainty from various uncertainty sources existing in the complex AM process [19]. Uncertainty quantifica-

tion (UQ) has attracted tremendous interest in many research areas including AM in order to dramatically improve product reliability and understand the intrinsic uncertainty associated with the computational model [19, 20]. Typical uncertainty sources include natural variation in powder absorptivity, fluctuation in temperature boundary, uncertainty in powder particle properties, and many others [21].

Conventional methods for simulating surface roughness and porosity rely on detailed powder scale simulations that account for irregular powder distributions and are restricted to deterministic simulations of small regions. Kumar et al. proposed a mathematical model that includes both presence of particles on top surfaces and the stair step effect for surface roughness prediction [22], while a data fusion approach for surface roughness prediction is made by Wu et al. in 2018 [23]. Powder bed metal additive manufacturing (PBMAM) porosity relies on parameters and was presented with a physics-based model by Ning et al. [24]. However, those models are computationally expensive and impede the consideration of part scale effects. Consequently, direct comparisons to engineering-size experimental measurements cannot be performed. Besides, the deterministic models with no stochastic information also restricts the prediction accuracy.

In this work, we propose a stochastic modeling strategy to significantly accelerate the computational time for surface roughness and porosity and can be used for part-scale AM simulations. More specifically, an effective physics-based stochastic model is developed. It allows part scale simulations to quantify uncertainties in AM processes and predict defects such as surface roughness and porosity of the as-built parts. In particular, Higher-Order Proper Generalized Decomposition (HOPGD) [25, 26], a specially designed tensor decomposition methods, is used as non-intrusive data learning and constructing reduced-order surrogate models for stochastic calibration. Experimental data [16], including melt pool measurements, is used to stochastically calibrate the heat source module on AM-CFD software (developed in-house) [12, 27]. The Markov Chain Monte Carlo (MCMC) sampling method is then used for the for statistical simulation predictions of process-structure-property that is capable of capturing the irregularities of LPBF scans. The proposed method has shown promise in predicting surface roughness and porosity for part scale simulations at very reduced computation costs while providing a high-fidelity computational model. Results for surface roughness, and porosity from this analysis tool will help provide highly accurate part scale property predictions that consider the inherent variation in melt pool geometry in AM processes.

The rest of the paper is organized as follows. Section 2 introduces the framework of physics-based stochastic AM model. Section 3 briefly describes the experimental methods as well as the probability distributions of data. In Section 4, physics-based stochastic model is built. Section 5 shows validation of the stochastic model and predict the surface roughness and porosity.

2. Proposed stochastic modeling framework for surface roughness and porosity prediction

The durability of AM parts has become an important topic to address for many applications, in which fatigue failure of materials has been one of the most common damage modes in cyclically loaded metallic materials. The fatigue life of AM parts is primarily governed by surface defects (e.g., surface roughness [28]) and volumetric structural defects (e.g., porosity [29]). We develop in this work effective stochastic physics-based models that will allow part scale simulations to predict surface roughness and porosity of the as-built parts. The overall framework is shown in Figure 1. Experimental data, including melt pool dimension measured from AFRL experiment top-down and cross-section images, will be used to stochastically calibrate the heat source module on AM-CFD code for thermal fluid analysis. In the AM-CFD simulation, some heat source parameters show strong uncertainties and will be further calibrated based on the experimental statistical distributions of melt pool data, where some statistical methods like the kernel density estimation [30] and Kullback–Leibler divergence [31] will be applied. To significantly reduce the computational cost for multi-parametric calibration, Higher-Order Proper Generalized Decomposition (HOPGD) [25, 26] is used to handle the model parameter calibration problem. The calibrated stochastic AM-CFD can then simulate part-scale samples using a Markov chain Monte Carlo (MCMC) method [32] by sampling the calibrated heat source parameters in different time series, with results better than deterministic models. The AM-CFD will be capable of predicting the surface roughness and lack-of-fusion (LOF) porosity of the as-built parts by simulating multilayer-multitrack models.

3. AFRL experimental data

3.1. Stochastic expression of experimental data

Laser powder bed fusion (LPBF) processes strongly trigger evaporation from the metal surface and the complex gas flow that disrupt the uniformity of the printed structure and subsequently result in properties of products. The computational model plays a significant role in understanding the process–structure–properties linkages in additive manufacturing (AM), and a well-designed experiment is required to ensure the accuracy of the models. In November 2019, the United States Airforce Research Laboratory: Materials and Manufacturing Directorate Structural Materials, Metals Branch (AFRL/RXCM) and America Made publicly announced the Additive Manufacturing Modeling Challenge Series, which provided a series of highly controlled additive manufacturing experiments for validation and quantification of computational models [33].

In the AFRL experiment, different cases including single-layer single-track, single-layer multi-track, and multi-layer single-track (thin-wall) builds of IN625 powder are produced with an EOS M280 commercial L-PBF system. To calibrate stochastic model, the single-track experiments with statistical measurements are used, while multi-track and multi-layer cases give validation to calibrated model and also measure

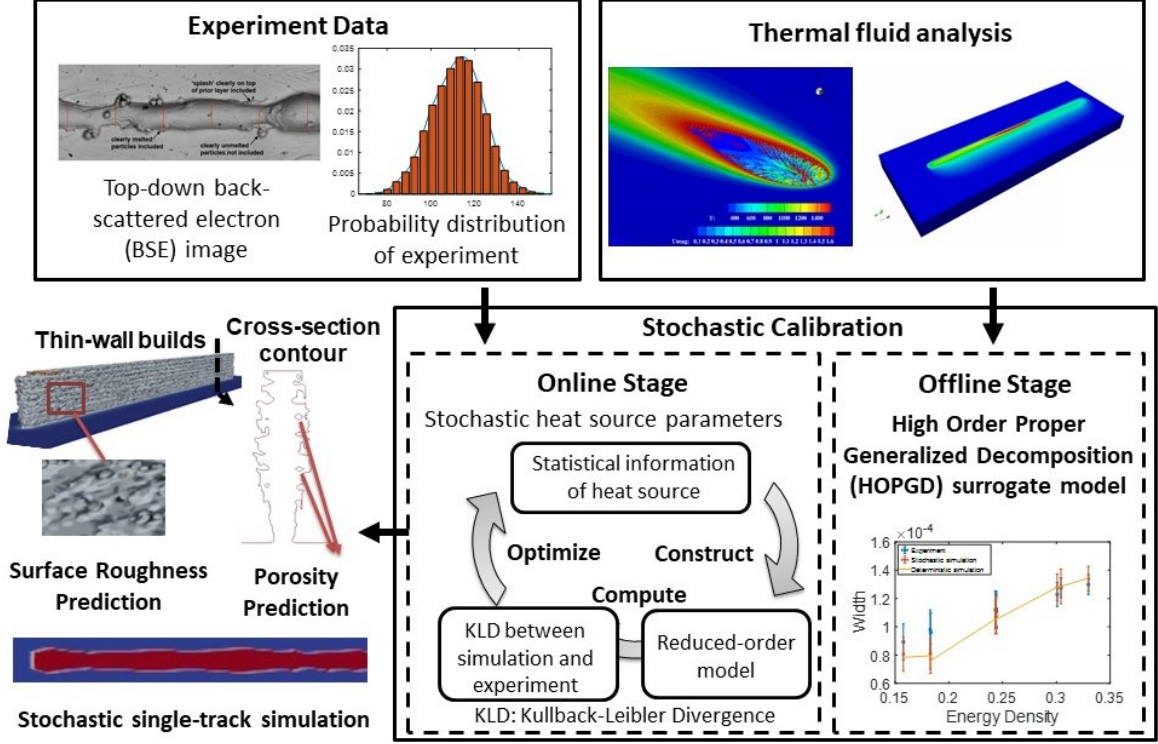


Figure 1: Stochastic additive manufacturing simulation framework

surface roughness and lack-of-fusion porosity. Measurements of melt pool dimensions were taken using a combination of electron backscatter diffraction, to obtain the top-down description of the track (Fig.2a) and optical microscopy on etched cross sections (Fig.2b). The full description of the experimental setups and measurement procedures can be found in reference.

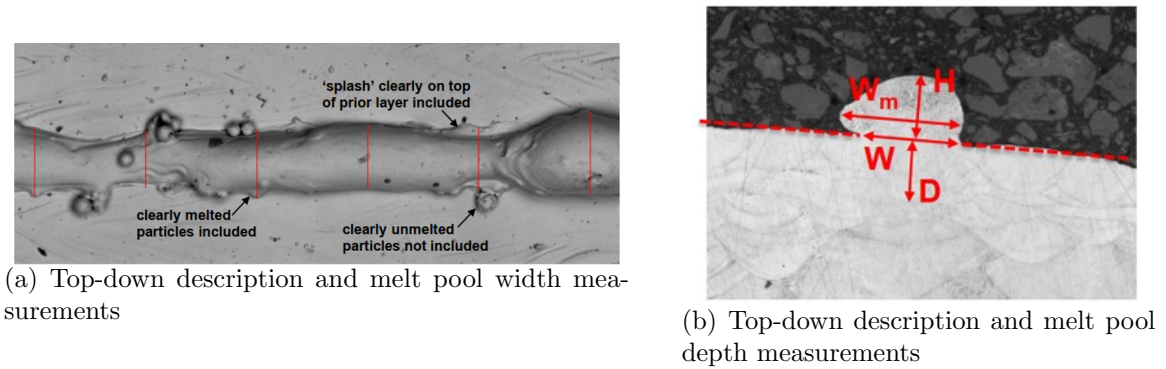


Figure 2: AFRL experiment measurements [33]: a) Top-down and b) cross-section melt pool description. In the top-down description, the red lines (Fig.2 a)) are samples of melt pool width measurements. In cross-section descriptions, W is the width of melt pool, W_m is the largest value of all widths, D and H are the depth and height of the deepest position of melt pool.

For identifying the best heat source parameters, it was necessary to know the influence of heat source parameters on the dimension. In particular, the width (measured

from top-down descriptions) and depth (the sum of D and H in cross-section images) of the single-track melt pool were the quantities of interest. Measured width and depth are shown in Table 1 and 2, where μ is the mean value and σ is the standard deviation.

Table 1: Width (μm) measurement for 11 single-track cases (A11-A11)

Case number	Laser Power (W)	Scan Speed (mm/s)	20 locations		30 locations		40 locations		50 locations	
			μ	σ	μ	σ	μ	σ	μ	σ
A1	300	1230	112.0 \pm 11.1		111.1 \pm 11.2		112.0 \pm 11.1		111.9 \pm 10.9	
A2	300	1230	112.0 \pm 11.9		111.1 \pm 11.2		112.0 \pm 11.1		111.9 \pm 10.9	
A3	290	953	127.6 \pm 7.0		124.7 \pm 9.1		125.5 \pm 10.5		125.5 \pm 10.0	
A4	370	1230	122.9 \pm 8.4		119.4 \pm 10.0		117.7 \pm 10.2		118.9 \pm 10.4	
A5	225	1230	96.0 \pm 13.9		100.1 \pm 14.2		99.7 \pm 13.1		99.9 \pm 13.3	
A6	290	1588	97.9 \pm 14.0		99.7 \pm 11.3		100.7 \pm 13.6		100.1 \pm 13.8	
A7	241	990	112.0 \pm 13.0		111.0 \pm 11.6		110.0 \pm 10.7		109.4 \pm 10.5	
A8	349	1430	110.7 \pm 11.3		113.3 \pm 11.6		113.7 \pm 11.0		113.4 \pm 11.3	
A9	300	1230	112.7 \pm 12.7		111.1 \pm 11.2		112.0 \pm 11.1		111.9 \pm 10.9	
A10	349	1058	129.9 \pm 7.0		128.3 \pm 9.7		127.5 \pm 9.8		127.3 \pm 9.4	
A11	241	1529	89.3 \pm 12.8		88.9 \pm 12.4		90.5 \pm 13.7		90.8 \pm 13.4	

Table 2: Depth (μm) measurement for 11 single-track cases (A1-A11)

Case number	Laser Power (W)	Scan Speed (mm/s)	Cross Section Height (AFRL)		Cross Section Height (this work)		Cross Section Depth (AFRL)		Cross Section Depth (this work)		Depth (sum)	
			μ	σ	μ	σ	μ	σ	μ	σ	μ	σ
A1	300	1230	59.1 \pm 12.3		59.0 \pm 12.9		54.3 \pm 9.0		54.3 \pm 8.9		113.3 \pm 13.4	
A2	300	1230	65.7 \pm 21.8		65.7 \pm 21.7		52.3 \pm 9.0		52.5 \pm 8.6		118.2 \pm 19.9	
A3	290	953	68.1 \pm 9.2		68.1 \pm 9.1		72.0 \pm 7.4		72.0 \pm 7.4		140.0 \pm 12.8	
A4	370	1230	66.0 \pm 15.5		66.2 \pm 15.3		75.9 \pm 7.6		75.9 \pm 7.2		142.1 \pm 17.4	
A5	225	1230	60.3 \pm 14.9		60.3 \pm 14.9		25.0 \pm 6.1		25.0 \pm 6.1		85.3 \pm 13.6	
A6	290	1588	62.2 \pm 18.3		62.2 \pm 18.4		26.9 \pm 5.4		27.1 \pm 5.6		89.3 \pm 19.9	
A7	241	990	61.2 \pm 11.9		61.2 \pm 11.9		42.5 \pm 6.6		42.6 \pm 7.2		103.8 \pm 13.2	
A8	349	1430	60.1 \pm 15.9		60.1 \pm 16.1		58.5 \pm 4.6		58.5 \pm 4.6		118.5 \pm 18.2	
A9	300	1230	68.8 \pm 25.9		68.8 \pm 26.0		46.9 \pm 9.3		46.8 \pm 8.8		115.5 \pm 30.6	
A10	349	1058	63.5 \pm 17.8		63.3 \pm 17.6		84.0 \pm 8.9		83.8 \pm 8.6		147.1 \pm 19.4	
A11	241	1529	56.3 \pm 18.1		56.3 \pm 18.3		20.1 \pm 7.1		20.1 \pm 7.1		76.4 \pm 22.1	

Table 1 indicates different location measurements of melt pool width, in which the forth column (20 locations) shows the result of AFRL measurement, while the fifth to seventh columns (30 to 50 locations) are measurements of this work. Similarly, comparisons of melt pool depth between AFRL and this work are shown in Table 2, while Depth (the last column) is the sum of cross-section depth and height.

3.2. Probabilistic model of the experimental data

To further calibrate the heat source model, probability density functions (PDF) of experimental melt pool dimensions width and depth are required and calculated from the measurement sample using Kernel Density Estimation (KDE), which is a

general and powerful way of estimating the probability density function of a random variable. A brief introduction of KDE is shown in the Appendix. The PDFs for 11 single-track experiment cases are shown in Fig.3.

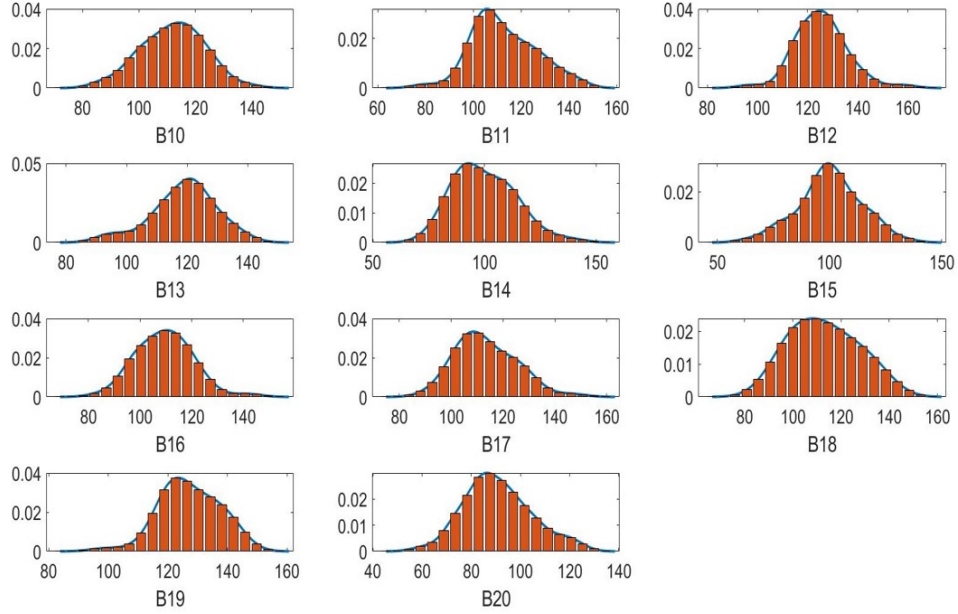


Figure 3: Experimental measurement (orange bar) and its probability density function generated by KDE (blue line) of single experiment case A1 to A11. x axis represents width, while y axis is probability density.

Figure 3 shows that the PDF generated by KDE matches well with experiment measurements, which will be further used to calibrated stochastic heat source parameters in the next section.

3.3. Basic Equations for thermal-fluid additive manufacturing

In this work, a thermal-fluid model considering liquid flow inside the melt pool driven by the Marangoni effect was developed as the AM process model to predict the melted track geometries of the L-PBF process. The basic theory of a well-tested transient three-dimensional thermal-fluid model that predicts the thermal field in the whole part and velocity field in the melt pool region is given. To solve the thermal-fluid model, the governing equations for mass, momentum, and energy conservation are given as follows: [34, 12]

$$\int_{\Omega_{f_l}} (\rho \nabla \cdot \mathbf{u}) dV = 0 \quad (1)$$

$$\int_{\Omega_{f_l}} \left(\frac{\partial(\rho \mathbf{u})}{\partial(t)} + \nabla \cdot \rho \mathbf{u} \mathbf{u} - \mu \nabla^2 \mathbf{u} + \nabla p + \frac{180\mu(1-f_l)^2}{c^2(f_l^3 + B)} \mathbf{u} - \rho_0 g \beta (T - T_0) \mathbf{I} \right) dV = 0 \quad (2)$$

$$\int_{\Omega} \left(\frac{\partial(\rho h + \rho \Delta H)}{\partial t} + \nabla \cdot (\rho \mathbf{u} h + \rho \mathbf{u} \Delta H + \nabla \cdot \mathbf{q}) \right) dV = 0 \quad (3)$$

where t is the time, \mathbf{u} is the velocity, μ denotes the viscosity, p is the pressure, T is the temperature, ρ is the density, and β is the thermal expansion coefficient. g is the acceleration of gravity and equals to 9.8 m/s^2 . ρ_0 and T_0 are density and temperature of reference material. H is the specific enthalpy, and can be divided into the sum of sensible heat h and the latent heat of fusion ΔH . In this paper, μ is set as a constant, c is the approximate primary dendritic spacing, which is set to $1 \text{ }\mu\text{m}$. B is used to avoid division by zero and set as $10^{-6}m$. f_l is the volume fraction of the liquid phase, which is defined as:

$$\begin{cases} f_l = 0 & \text{if } T \leq T_s \\ f_l = \frac{T - T_s}{T_l - T_s} & \text{if } T_s < T < T_l \\ f_l = 1 & \text{if } T \geq T_l \end{cases} \quad (4)$$

where T_s and T_l are the solidus and liquidus temperature of materials, respectively.

Considering $\bar{\mathbf{q}}$ on the surface boundary, heat flux \mathbf{q} and its relation with temperature T is

$$\mathbf{q} = -\mathbf{k} \cdot \nabla T \quad (5)$$

where \mathbf{k} is the thermal conductivity tensor. In isotropic cases, $\mathbf{k} = k\mathbf{I}$ denotes the second-order identity tensor. The heat source and boundary condition can be written as:

$$\begin{cases} \bar{\mathbf{q}} \cdot \mathbf{n} = h_c(T - T_0) - \sigma_s \varepsilon (T^4 - T_0^4) + q_{source} & \text{on } \partial\Omega_q \\ T = \bar{T} & \text{on } \partial\Omega_q \end{cases} \quad (6)$$

where h_c defines the convective heat transfer coefficient, σ_s is the Stefan–Boltzmann constant, ε is the emissivity, \mathbf{n} is the normal direction of heat source surface.

The heat source q_{source} from the laser, is described by a cylindrical shape with a Gaussian distribution described below:

$$q_{source} = \begin{cases} \frac{\epsilon Q \eta}{\pi r_b^2 d} \exp\left(\frac{-2(x_b^2 + y_b^2)}{r_b^2}\right) & z_{top} - z \leq d; \\ 0 & z_{top} - z > d \end{cases} \quad (7)$$

where Q denotes the flux intensity, ϵ denotes the intensity factor, η is the absorptivity, r_b is the laser beam radius, d is the depth of the heat source, and z_{top} is the z-coordinate of the top surface of the computational domain. x_b and y_b are the coordinates in the local reference system attached to the moving heat source. Note that the parameters, η , r_b and d , are all unknown and uncertain variables, which are highly correlated to the vapor depression phenomenon in the L-PBF process. During calibration, the minimum value of absorptivity is limited to 0.28[35]. It is reported from the literature [35, 36] that as the laser power increases or the scan speed decreases, a vapor-induced depression appears and deepens, which leads to higher absorptivity caused by multiple

reflections of the laser beam between the liquid and gas interface. Thus, we assume the three parameters, η , r_b and d are related to the ratio of laser power P to scan speed V , shown as:

$$d = P1 \frac{P}{V} \quad (8)$$

$$\eta = \max(P2 \frac{P}{V}, 0.28) \quad (9)$$

$$r_b = P3 \frac{P}{V} \quad (10)$$

$P1, P2, P3$ are three unknown parameters which require calibration using HOPGD method (described in section 4.1). The boundary condition for Eq.2 at the top surface is equal to the surface tension (i.e. Marangoni force):

$$\tau_x = \mu \frac{\partial u_x}{\partial z} = \frac{d\gamma}{dT} \nabla_x T \quad (11)$$

$$\tau_y = \mu \frac{\partial u_y}{\partial z} = \frac{d\gamma}{dT} \nabla_y T \quad (12)$$

where γ is the surface tension, which depends on both temperature and materials, and $\frac{d\gamma}{dT}$ is the temperature coefficient.

The powder layer is treated as a continuous media, and it is distinguished from the substrate through its material properties. A consolidated factor α ranging from 0 to 1 is used to identify the material state. The value of 0 stands for the material is in the original powder state (no consolidation), while 1 denotes a bulk state (fully consolidated). The definition of α is:

$$\alpha = \frac{T_{peak} - T_s}{T_l - T_s} \quad (13)$$

where T_{peak} is the local peak energy, and T_s and T_l are solid and liquid temperature of material, respectively.

The thermophysical properties of IN625 are summarized in Table 3. The densities at ambient and liquidus temperatures are used for solid and liquid densities, respectively. Temperature-dependent polynomials were used for the solid's thermal conductivity and solid's specific heat capacity.

In order to consider the influence of the localized preheating from adjacent scan paths that leads to transient behavior of the vapor depression, the residual heat factor (RHF) is considered into the heat source model [40]. RHF at specific point i is defined as:

$$RHF_i = \sum_{k \in S_i} \left(\frac{R - d_{ik}}{R} \right)^2 \left(\frac{T - t_{ik}}{T} \right) L_k \quad (14)$$

The scan path is composed of discrete points defined by the time step of the simulation and the laser scan speed. d_{ik} denotes the distance between point

Table 3: Thermo-physical properties of IN625 and process constants [33, 37, 38, 39]

Property/parameter	Value	Property/parameter	Value
Solid density ($kg\ m^{-3}$)	8440	Convection coefficient ($W\ m^{-1}\ K^{-1}$)	10
Liquid density ($kg\ m^{-3}$)	7640	Latent heat of fusion ($KJ\ kg^{-1}\ K^{-1}$)	290
Powder density ($kg\ m^{-3}$)	4330	Dynamic viscosity ($Pa\ s$)	710^{-3}
Solidus temperature (K)	1563	Thermal expansivity ($1/K$)	510^{-5}
Liquidus temperature (K)	1623	Surface tension ($N\ m^{-1}$)	1.8
Solid specific heat capacity ($J\ kg^{-1}\ K^{-1}$)	$0.2441T + 338.39$	Marangoni coefficient ($N\ m^{-1}\ K^{-1}$)	-3.810^{-4}
Liquid specific heat capacity ($J\ kg^{-1}\ K^{-1}$)	709.25	Emissivity	0.4
Powder specific heat capacity ($J\ kg^{-1}\ K^{-1}$)	$0.2508T + 357.70$	Ambient temperature (K)	295
Solid thermal conductivity ($W\ m^{-1}\ K^{-1}$)	$0.0163T + 4.5847$	Reference temperature (K)	295
Liquid thermal conductivity ($W\ m^{-1}\ K^{-1}$)	30.078	Preheat temperature (K)	353
Powder thermal conductivity ($W\ m^{-1}\ K^{-1}$)	0.995	Stefan-Boltzmann constant ($W\ mm^{-2}\ K^{-4}$)	5.6710^{-14}

i and k , which indicates the preheating on point i by a previously scanned point k . Similarly, elapsed time since k was scanned is denoted by t_{ik} . L_k , the normalized laser power at point k , is equal to 1 when the laser is on, while 0 denotes the laser is off. R and T are constants with the values of 2×10^{-4} and 2×10^{-3} , respectively. They play as thresholds that ignore points which had not interacted with the laser for a sufficient amount of time, while the other points within the threshold belong to set S_i , where $S_i = \{t_{ik} < T \cup d_{ik} < R, \text{ where } i > k\}$. RHF is normalized as $RHF = \frac{RHF_i}{RHF_c}$, where RHF_c equals to RHF_i at the middle part of the toolpath, and it is greater than 1 at the corner of the toolpath, as shown in the flowing figure.

Considering the influence of residual heat, the heat source parameters can be coupled with the RHF as:

$$d = P1 \frac{P}{V} RHF^2 \quad (15)$$

$$\eta = \max(P2 \frac{P}{V} RHF^2, 0.28) \quad (16)$$

$$r_b = P3 \frac{P}{V} RHF^2 \quad (17)$$

where three unknown parameters $P1$, $P2$, $P3$ will be further calibrated with HOPGD method.

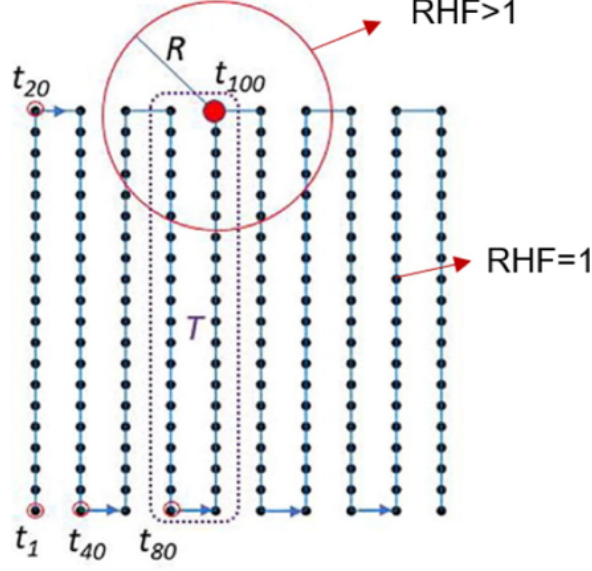


Figure 4: Quantitative comparisons of cross-sectional area between experimental measurements and stochastic simulation [40]

4. Stochastic calibration for process parameters

The Higher-Order Proper Generalized Decomposition (HOPGD) based data-driven reduced order model is used to do stochastic calibration for process parameters to find the interaction between the metal and the laser heat source.

4.1. Tensor decomposition based surrogate model

One challenge for accurate AM simulations is the identification of model parameters. One standard way for unknown parameters calibration is the genetic algorithm approach, in which evaluation of parameters requires repeated calls of the computational model. This results in high computational costs, and thus, a HOPGD-based reduced order surrogate model is used to accelerate the parameter calibration (identification) process significantly.

HOPGD, a non-intrusive data learning and constructing reduced order surrogate models, relies on the database and falls into the family of data-driven approaches. The database can be either from simulations or experiments, and the foundation behind tensor decomposition is the separation of variables technique. For a n -dimensional function $f(\mu_1, \mu_2, \mu_3, \dots, \mu_n)$ that contains the quantity of interest as a function of n parameters, HOPGD separation form is:

$$f(\mu_1, \mu_2, \mu_3, \dots, \mu_n) \approx \sum_{m=1}^k F_1^{(m)}(\mu_1) F_2^{(m)}(\mu_2) F_3^{(m)}(\mu_3) \dots, F_n^{(m)}(\mu_n) \quad (18)$$

The function f is given by the finite sum of products of the separated functions $F_i^{(m)}(i = 1, \dots, n)$. $F_i^{(m)}$ identifies the variation of function f in the parameter direction μ_i , which is also called mode function. n is the rank of approximation and m defines

the mode number of each component (not represent exponential terms). The number of n is priori unknown and can be obtained with a precomputed physics-based simulation database [25, 26, 41, 42]. HOPGD seeks the projection of data for computing the mode functions that can reproduce the original function, and thus can be used as a surrogate model for fast prediction. Examples of codes can be found on the GitHub project (<https://yelu-git.github.io/hopgd/>).

In our AM computational model, we seek to identify the relations between heat source model and important parametric melt pool dimensions (width and depth), unknown parameters are calibrated with the following HOPGD model:

$$Y_s = \begin{bmatrix} W_s \\ D_s \end{bmatrix} \approx \begin{bmatrix} W_{PGD} \\ D_{PGD} \end{bmatrix} = F(e, P1, P2, P3) = \sum_{m=1}^k F_1^{(m)}(e) F_2^{(m)}(P1) F_3^{(m)}(P2) F_4^{(m)}(P3) \quad (19)$$

where $P1, P2, P3$ are heat source parameters, $e = \frac{P}{V}$ is the energy density. Note that all parameters in this section are deterministic. W_s and D_s are melt pool dimensions width and depth calculated from simulation. W_{PGD} and D_{PGD} are predictions of width and depth from the HOPGD surrogate model. Once the HOPGD surrogate model is constructed, real time predictions can be used in an optimization problem to find calibrated parameters p^* . The optimization problem for the calibration can be written as

$$p^* = \arg \min [J(W_{PGD}, W_e, p) + J(D_{PGD}, D_e, p)] \quad (20)$$

where W_e and D_e are AFRL single-track width and depth measurements. $p = [P1, P2, P3]$, and J denotes the objective function that measures the distance between the surrogate model's predictions and the experimental measurements. The above surrogate model used significantly reduce the computational cost, since only 1D interpolation is required to find output of a given point after finding functions $F_i^{(m)}$. The method is applicable to deal with high-dimensional problems with limited costs, which is challenging for other methods.

The steps to solve the optimization problem in Eq.20 are:

1. Sample the parameter space with the adaptive sparse grid strategy [26, 43] and compute the simulated melt pool dimensions (W_s, D_s) with the AM-CFD model for the selected data points.
2. Construct HOPGD surrogate model and calculate W_{PGD} and D_{PGD} with Eq.19 for sample data.
3. Solve the optimization problem in Eq.20 with HOPGD surrogate model to calibrate heat source parameters.

4.2. Stochastic calibration for heat source parameters

Section 4.1 shows the framework of building a surrogate model and a deterministic strategy to calibrate process parameters. To further indicate surface roughness and porosity in the L-PBF process, stochastic heat source parameters which contains noise

information are required to be calibrated. The stochastic calibration can be based on the same HOPGD model presented previously.

This time, the stochastic heat source parameters are assumed to satisfy a tri-variate normal distribution:

$$p(P1, P2, P3) = \frac{1}{(2\pi)^{\frac{3}{2}} |\Sigma|^{\frac{1}{2}}} e^{-\frac{1}{2}[(P-\mu)^T \Sigma^{-1} (P-\mu)]} \quad (21)$$

where $P = [P1, P2, P3]^T$ is the vector of heat parameters, $\mu = [\mu1, \mu2, \mu3]^T$ is the mean vector. $\Sigma = \begin{bmatrix} C11 & C12 & C13 \\ C21 & C22 & C23 \\ C31 & C32 & C33 \end{bmatrix}$ is the covariance matrix. Due to the symmetry of Σ , unknown coefficients are $\mu_1, \mu_2, \mu_3, C_{11}, C_{22}, C_{33}, C_{12}, C_{23}, C_{13}$ whose distributions are required to be calibrated. The calibrated stochastic AM-CFD can then simulate part-scale samples using Markov chain Monte Carlo method. The stochastic AM-CFD will be capable of predicting the surface roughness and lack-of-fusion (LOF) porosity of the as-built parts by simulating multilayer-multitrack models.

Similar to the processes of finding the distribution of experimental W_e and D_e ($f_{W_e}(x)$ and $f_{D_e}(x)$), the distributions of W_{PGD} and D_{PGD} ($f_{W_{PGD}}(x)$ and $f_{D_{PGD}}(x)$) are also estimated with kernel density estimation. An optimization problem is defined to calibrate the stochastic parameters:

$$p^* = \arg \min [J(W_{PGD}, W_e, p) + J(D_{PGD}, D_e, p)] \quad (22)$$

W_e and D_e are statistical experimental measurements that with mean and variance. Besides, W_{PGD} and D_{PGD} in Eq.22 also satisfy statistic distributions which are calculated based on stochastic parameters P1,P2,P3 in Eq.15. To define the distance J between different melt pool distributions, Kullback-Leibler Divergence (KLD) [31] will be introduced, which is required in the optimization of calibrated parameters. A brief introduction of Kullback-Leibler Divergence is in Appendix.

KLD enables to qualify the distance between two distributions. If the KLD reaches the minimum, the probability density estimation expression can be considered to achieve its best estimation result. Thus, the objective function in Eq.22 can further be defined with KLD:

$$p^* = \arg \min \sum_{i=1}^{11} f_{W_e(i)}(W_e) \log \frac{f_{W_e(i)}(W_e)}{f_{W_{PGD}(i)}(W_{PGD}(P1, P2, P3))} + \sum_{i=1}^{11} f_{D_e(i)}(D_e) \log \frac{f_{D_e(i)}(D_e)}{f_{D_{PGD}(i)}(D_{PGD}(P1, P2, P3))} \quad (23)$$

where i is the index of single-track cases. $f_{W_e}, f_{D_e}, f_{W_{PGD}}, f_{D_{PGD}}$ are distributions of experimental width, experimental depth, simulated width and depth with HOPGD surrogate model, respectively.

The distributions of experiment and simulation can be obtained through KDE [30]:

$$f_{WPGD(i)}(W) = \frac{1}{nh} \sum_{j=1}^n K\left(\frac{W - W_{PGDj}}{h}\right) \quad (24)$$

$$f_{DPGD(i)}(D) = \frac{1}{nh} \sum_{j=1}^n K\left(\frac{D - D_{PGDj}}{h}\right) \quad (25)$$

$$f_{We(i)}(W) = \frac{1}{nh} \sum_{j=1}^n K\left(\frac{W - W_{ej}}{h}\right) \quad (26)$$

$$f_{De(i)}(D) = \frac{1}{nh} \sum_{j=1}^n K\left(\frac{D - D_{ej}}{h}\right) \quad (27)$$

where k is the Gaussian kernel. n is the number of sample points and h is the bandwidth. Detailed expression are shown in the appendix.

5. Validated melt-pool geometry prediction against AFRL experimental data

In this section, different single-track, multi-track and multi-layer cases are validated with AFRL experimental data using the stochastic AM simulation model.

5.1. Stochastic prediction of single-track melt pool

The stochastic simulation model in the previous section enables to predict uncertainty of LBPF melt pool with stochastic process parameters and heat source parameters. To predict stochastic single-track melt pool, Markov Chain Monte Carlo (MCMC) [32], an algorithms for sampling from probability distributions based on time series, is used for samples generation and statistical simulation predictions of process-structure-property.

In each fluid dynamics time step, MCMC-sampled heat sources is imported into AM-CFD program, which helps for predicting surface roughness and porosity for part scale simulations at very reduced computation costs while providing a high-fidelity computational model. The comparisons between experiment, deterministic simulation (with constant heat source model), and stochastic simulation (with calibrated stochastic heat source model) is shown below.

The comparisons of overall geometry (Figure 5) and cross-section view (Figure 6) between deterministic and stochastic simulation is shown. Clear uncertain information is revealed in stochastic AM simulation. To verify the accuracy of stochastic simulation, statistical information (e.g. mean and variance for melt pool width and depth) between stochastic simulation, and experiment [33] are summarized in Figure 6 and 7.

In figure 6 and 7, energy density for 11 different single-track cases are shown in x coordinates, while y coordinates present the melt pool width and depth, respectively. The blue and red error bars show mean and variance of experiment and stochastic simulation. The yellow line passes through the deterministic simulation melt pool

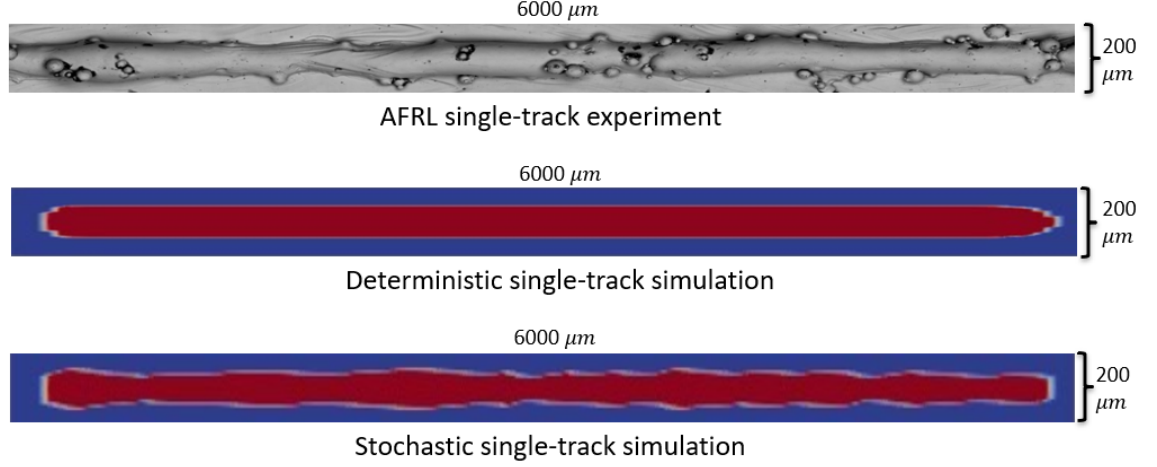


Figure 5: Comparisons between AFRL experiment [33], deterministic simulation (with constant heat source model), and stochastic simulation (with calibrated stochastic heat source model) for single track

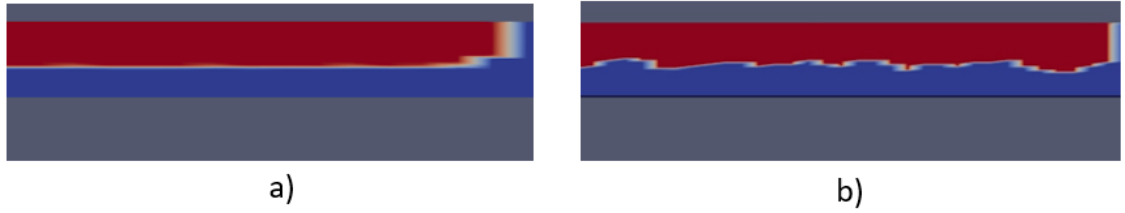


Figure 6: Cross-section view comparisons between a) deterministic simulation and b) stochastic simulation for single track

dimensions. Cases with close energy density are zoomed in for detailed comparison. To calculate the mean and variance of melt pool dimensions, 50 width locations and 20 depth locations are measured from experiments and stochastic simulations. It can be seen from figure 6 and 7 that the stochastic simulation matches well experiment melt pool dimensions. Compared with deterministic simulation, stochastic simulation contains uncertain information of melt pool and show more accurate predictions for most cases.

5.2. Validation of multilayer and multi-track cases

To further predict surface roughness and porosity, multi-layer (thin-wall) and multi-track cases are also simulated with stochastic AM-CFD model.

The simulation of two thin-wall specimens, B1 and B2, consists of 10 consecutive 40 μm thick layers each with a unidirectional scanning track length of 5 mm [33]. One of the thin walls used a laser power of 300 W and a scan speed of 1230 mm/s, whereas the other used 241 W and 1529 mm/s as shown in Table 4. Figure 8a shows the simulated result for case B1. For a quantitative comparison, the wall is divided into three measurement zones shown in Figure 8a. The average and standard deviation of the height above the substrate pad datum and the total cross-sectional

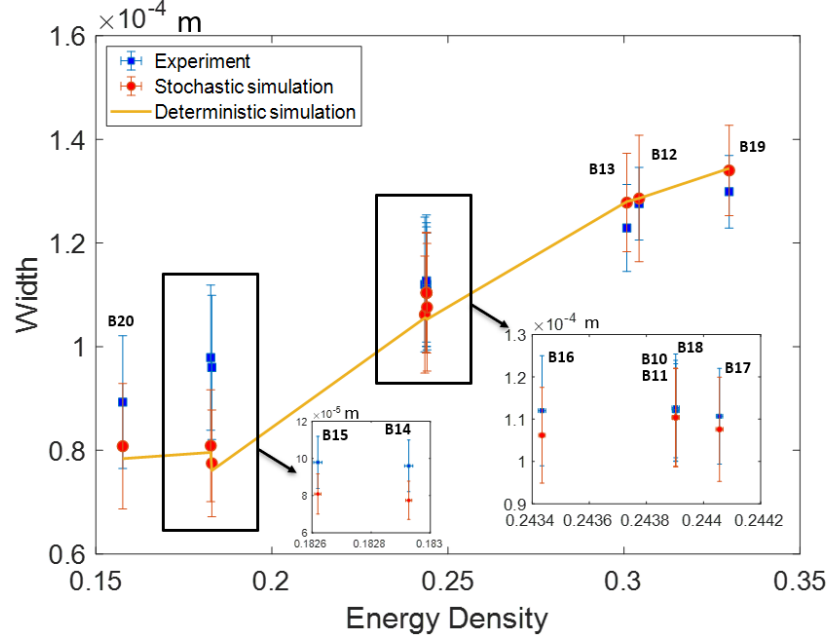


Figure 7: Statistical information of melt pool width between stochastic simulation, deterministic simulation and experiment

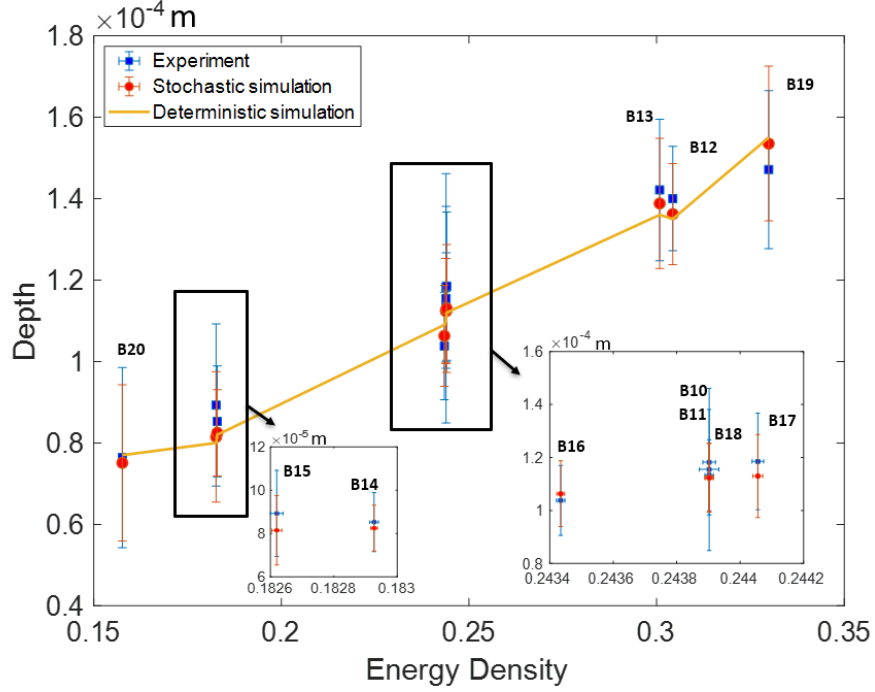


Figure 8: Statistical information of melt pool depth between stochastic simulation, deterministic simulation and experiment

area for the entire portion of the wall above the substrate pad datum were measured for each measurement zone as shown in Fig. 8b. There is a minimum of 3 cross sections collected within Zones 1 and 3, and approximately 20 cross sections in Zone 2.

Table 4: Multi-layer simulation process parameters [33]

Case Number	Laser Power (W)	Scan Speed (mm/s)	Layer thickness (μm)	Track length (mm)	The number of layers
B1	300	1230	40	5	10
B2	241	1529	40	5	10

Figure 9 shows the comparisons of the cross sectional area for the three different zones between the experimentally measured and computationally predicted for B1 and B2 multi-track cases. The simulated height and area match well with the measurements in the second and third zones, which indicates the developed model can predict the steady-state melt pool geometry well. However, at Zone 1, the beginning region of each layer, the model underestimates the results. This implies that some transient behaviors occurring at the beginning of each layer are being neglected by the model.

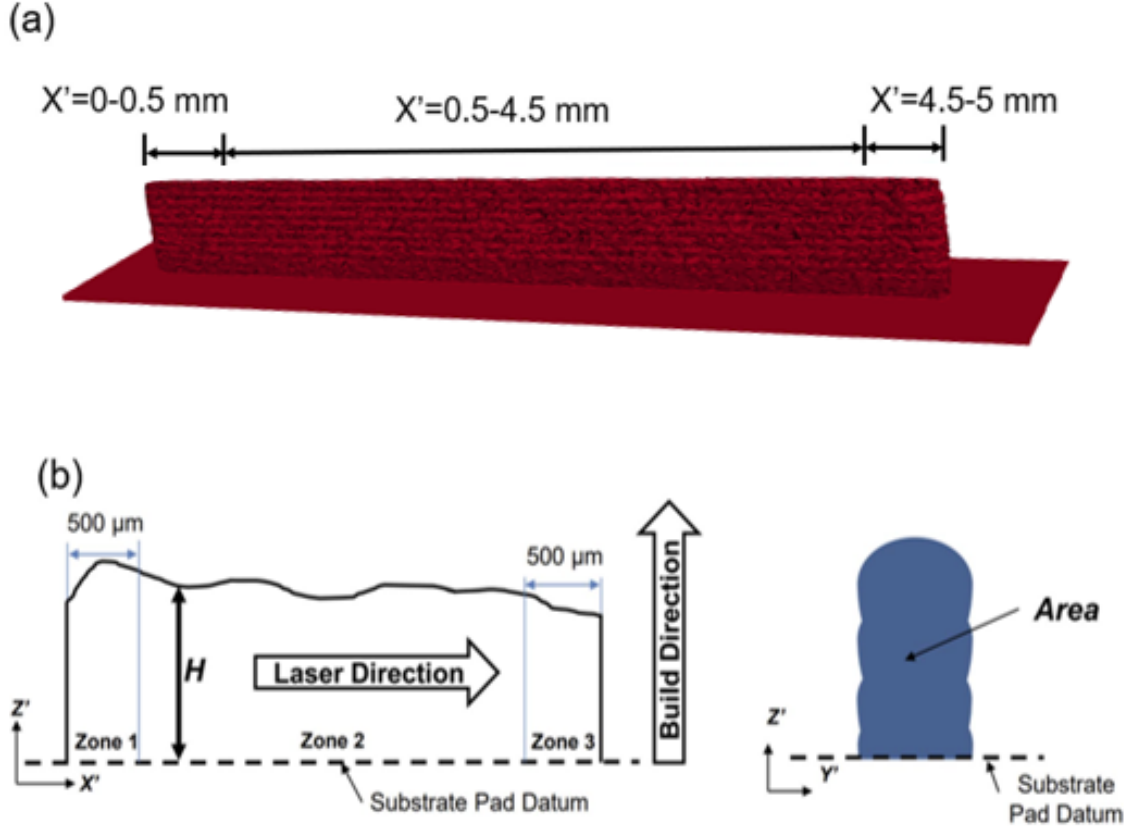


Figure 9: As-built multi-layer structure and its measurements for case B1. a) Multi-layer simulation. b) A schematic of the cross section area measurements for three Zones [33]

Six multi-track cases are also simulated with calibrated stochastic AM-CFD model to predict geometrical details of the melted tracks for the L-PBF process. Figure 10 indicates the substrate geometries and tool paths of those six simulations (multi-track cases C1, C2, C3, C4, C5, and C6). The tool paths are labeled according to

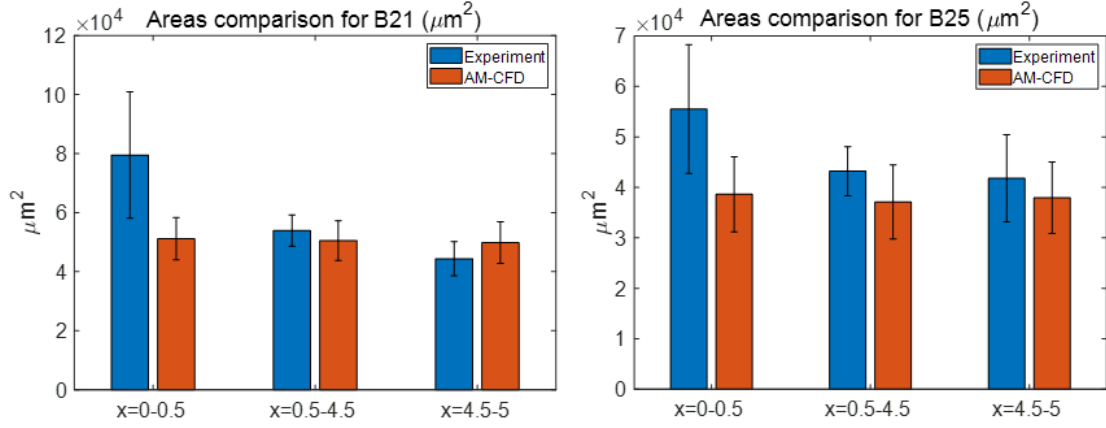


Figure 10: Quantitative comparisons of cross-sectional area between experimental measurements and stochastic simulation

Table 5: Multi-track simulation process parameters [33]

Case Number	Laser Power (W)	Scan Speed (mm/s)	Hatch Spacing (mm)	Toolpath plane dimensions (mm)	The number of tracks
C1	300	1230	0.1	3*3	30
C2	300	1230	0.1	10*3	30
C3	300	1230	0.075	10*3	40
C4	300	1230	0.125	10*3	24
C5	300	1230	0.1	10*3	30
C6	290	953	0.1	15*3	30

the L-PBF experiments performed by AFRL. A dwell time of 0.5ms is set in which the laser beam is turned off while the beam moves to the beginning position of the next scan path. The black frames show the substrate dimensions, and the arrows represent the laser scan paths. Table 5 summaries the process parameters used for all 6 multi-track cases. Quantitative comparisons of melted track geometries between experiment, deterministic and stochastic at the middle of the toolpath ($x=1.5\text{mm}$) for multi-track simulation C1 is shown in Figure 11 a) . The average and standard deviation of each quantity for the tracks are plotted and W defines the melt pool width and D stands for the melt pool depth, which are defined in Figure 11 b). The multi-track simulations matches well with experimental data, and have shown promise in high-precision AM predictions with incapability of capturing the variation in melt pool, which can further give potentials in predicting surface roughness and porosity for part scale simulations at very reduced computation costs.

6. Stochastic thermal-fluid additive manufacturing simulation based surface roughness and porosity prediction

Fatigue failure plays an significant role in the durability of AM parts. The fatigue life of AM parts is primarily governed by surface defects (e.g., surface roughness) and volumetric structural defects (e.g., porosity). However, generally, the simulation of

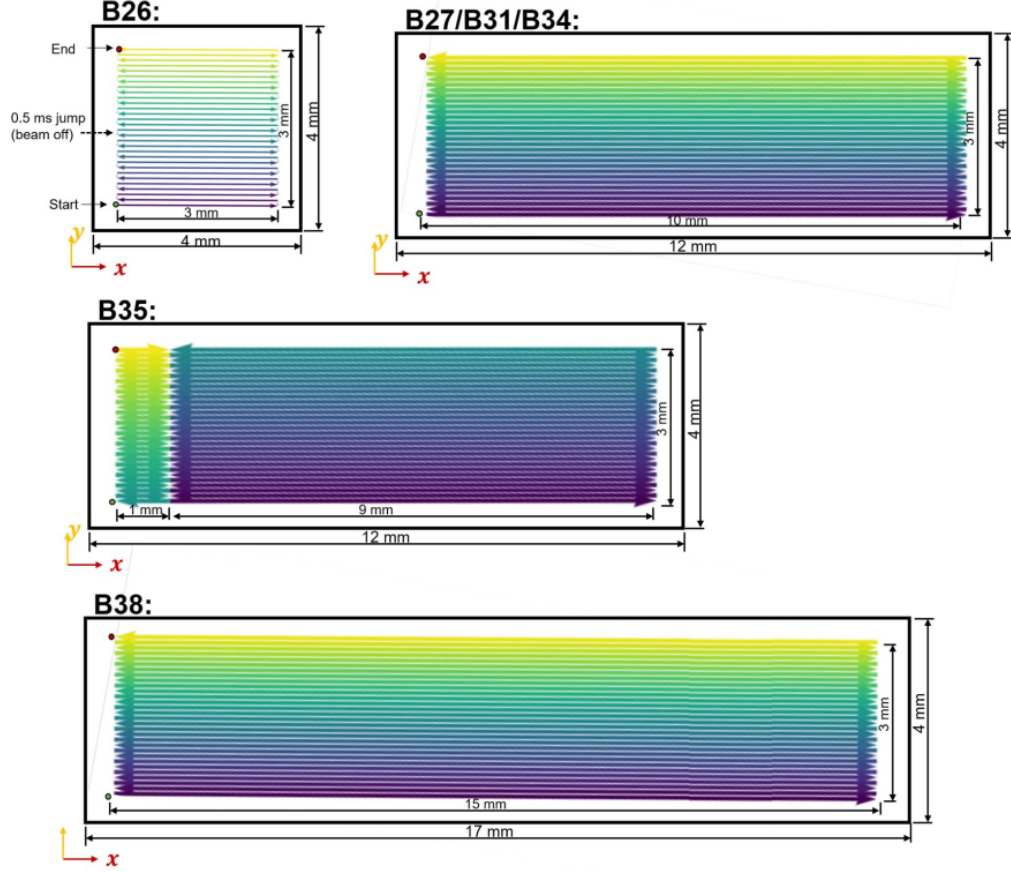


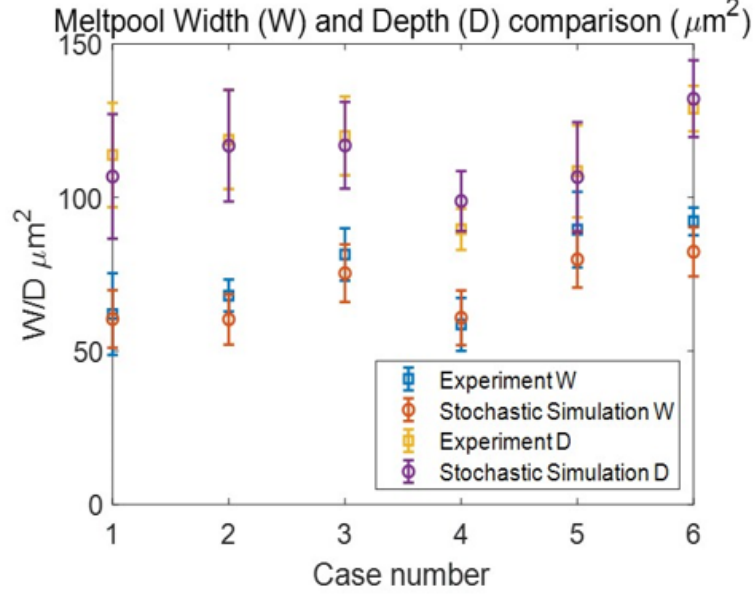
Figure 11: Surface roughness and porosity for multi-layer simulation [33]

surface roughness or porosity are very difficult because of the lack of simulation model which is able to describe uncertain information accurately in statistical level but still simple enough to satisfy the efficiency requirement at the same time. Thanks to the validated stochastic physics-based AM-CFD model shown in the previous sections, we are capable of predicting the surface roughness and lack-of-fusion (LOF) porosity of the as-built parts by simulating multilayer-multitrack models, as shown below. To generate time-dependant sequences, Markov chain Monte Carlo method is used for part-scale sampling of the calibrated stochastic AM-CFD model.

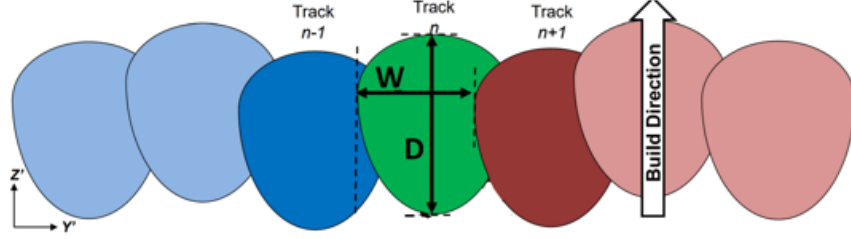
6.1. Prediction of surface roughness

Figure 12 shows the multi-layer simulation which clearly indicates the surface roughness and porosity. The rest of this section shows how to measure the surface roughness and compared it with experimental results.

The main roughness parameters reported is average roughness (R_a). It evaluate the average standard deviation of the heights (valleys and peaks) in a surface profile to compute the degree of roughness. For the computation of these parameters, it is first necessary to compute the fitting plane for the points acquired from the surface. From the plane coefficients, it is possible to determine the height of a peak or valley by evaluating the height coordinate of each point of the cloud.



a)



b)

Figure 12: Quantitative comparisons of melt pool dimensions between experimental and stochastic simulations, a) W and D are melt pool width depth, respectively. The average and standard deviation of each quantity for different tracks are plotted (The error bar represents the standard deviation.)

The equation of average roughness Ra is given by [44]:

$$Ra = \frac{1}{A} \iint_S |f(y)| dS \quad (28)$$

where A is the sampling area and $f(y)$ is height of the profile. The simulated wall is equally divided into 10 regions, and the mean value and variance of multilayer cases B1 and B2 cases are thus calculated by considering different regions (B1: $Ra = 12.62 \pm 2.21 \mu m$, B3: $Ra = 14.57 \pm 2.78 \mu m$)

Surface roughness experiments [45] are used to validate the simulated surface roughness. In the experiment, the same material as AFRL Challenge2 is used (IN625), and the relation between surface roughness and volumetric energy density (VED) [46] is given. Different from linear energy density e in the previous section, the equation for VED is:

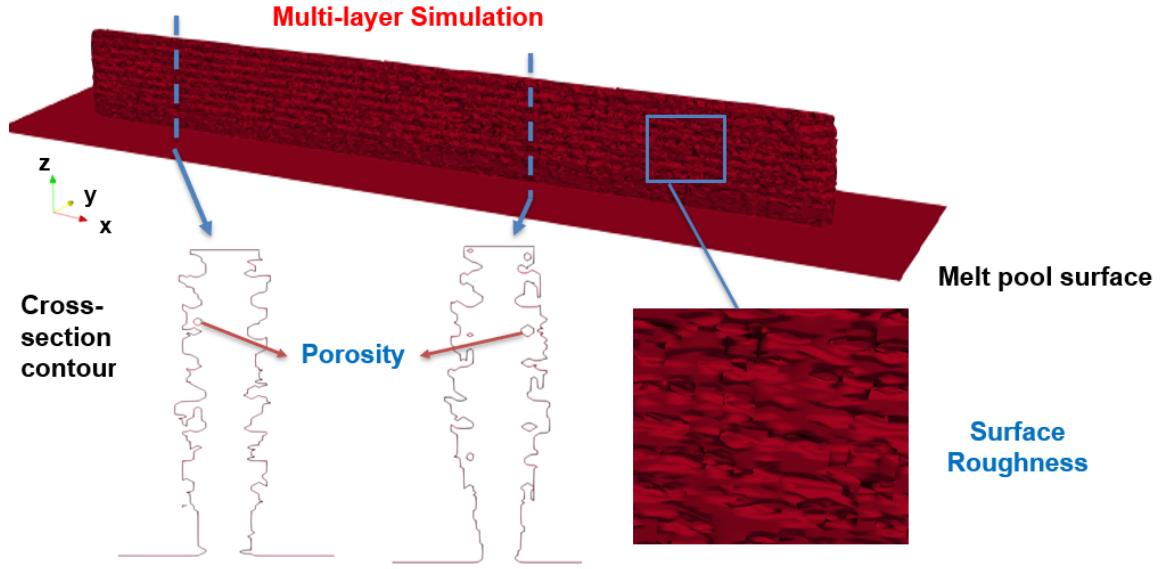


Figure 13: Surface roughness and porosity for multi-layer simulation

$$VED = \frac{P}{V\sigma t} \quad (29)$$

where P is laser power, V is scan speed, σ is the laser beam diameter, and t is the thickness for a single layer. VEDs for B1 and B2 multi-layer cases are in the following table, and the comparisons between experiment and simulation surface roughness are in Figure 11.

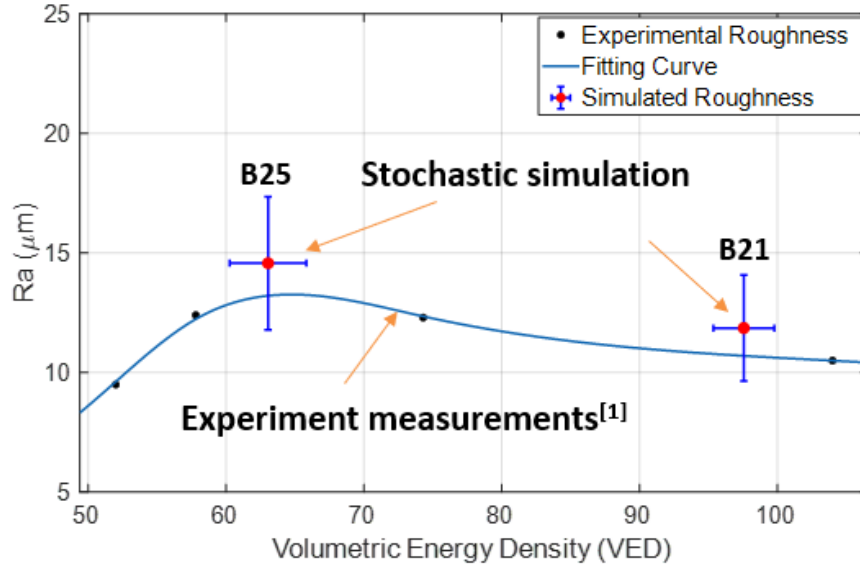


Figure 14: Surface roughness and porosity for multi-layer simulation

In figure 13, the black dots are the experiment roughness with different VEDs.

The blue curve is the fitting curve of experiment surface roughness. The two error bars are the simulated roughness with corresponding mean and variance for B1 and B2. The comparison shows the simulated roughness match well with experiment, which validate the accuracy of the stochastic AM simulation.

7. Conclusion

In this paper, an effective physics-based stochastic modeling framework is proposed for LPBF simulations. Non-intrusive data learning method, including Higher-Order Proper Generalized Decomposition (HOPGD), is used for constructing reduced-order surrogate models for stochastic calibration. The Markov Chain Monte Carlo (MCMC) sampling method is then used for the for statistical simulation predictions of process-structure-property that is capable of capturing the irregularities of LPBF scans. The stochastic simulation predictions are validated against AFRL multi-layer and multitrack experiments. The results are more accurate when compared with regular deterministic simulations. The proposed method has shown promise in predicting surface roughness and porosity for part scale simulations at very reduced computation costs while providing a high-fidelity computational model. Results for surface roughness, and porosity from this analysis tool will help provide highly accurate part scale property predictions that consider the inherent variation in melt pool geometry in AM processes.

Acknowledgements

The authors would like to acknowledge the support of NSF Grant CMMI-1934367.

Appendix A. Kernel Density Estimation [30]

Kernel Density Estimation (KDE), a general and powerful way of estimating the probability density function of a random variable, is used to find the distribution of experimental data, which will be used to calibrate the stochastic simulation process parameters. The density function can be estimated through the first derivative of the distribution function. One of the simplest and most effective methods for estimating distribution functions is the so-called Empirical Distribution Function (EDF). That is, the estimate of $F_n(t)$ is the probability of all samples less than t :

$$F_n(t) = \frac{\text{The number of elements in the sample} \leq t}{n} = \frac{1}{n} \sum_{i=1}^n \mathbf{1}_{w_i \leq t} \quad (\text{A.1})$$

where $\mathbf{1}_{w_i \leq t}$ is the indicator function. The indicator function of a subset A of a set W is defined as:

$$\mathbf{1}_A(w) = \begin{cases} 1 & \text{if } w \in A \\ 0 & \text{if } w \notin A \end{cases} \quad (\text{A.2})$$

EDF is not differentiable and not smooth enough to compute the density function by the first derivative with respect to EDF. Thus, central difference can be used to find the density function:

$$f(w) = \lim_{h \rightarrow 0} \frac{F(w+h) - F(w-h)}{2h} \quad (\text{A.3})$$

Replace the distribution function with the empirical distribution function in Eq.A.1, the numerator of Eq.A.3 is the number of points falling in the interval $[w-h, w+h]$, which can be written as:

$$f(w) = \frac{1}{2Nh} \sum_{i=1}^N \mathbf{1}(w-h \leq w_i \leq w+h) = \frac{1}{Nh} \sum_{i=1}^N \frac{1}{2} * \mathbf{1}\left(\frac{|x-x_i|}{h} \leq 1\right) \quad (\text{A.4})$$

where N is the number of sample points and h is the bandwidth. If so-called kernel function $K(t) = \frac{1}{2} * \mathbf{1}(t \leq 1)$ is used, Eq. A.4 can be further written as:

$$f(w) = \frac{1}{Nh} \sum_{i=1}^N K\left(\frac{w-w_i}{h}\right) \quad (\text{A.5})$$

Eq.A.5 gives the expression of KDE, which is also the estimation of probability density function. The integration of Eq.A.5 is:

$$\int f(w) dw = \frac{1}{Nh} \sum_{i=1}^N \int K\left(\frac{w-w_i}{h}\right) dw = \frac{1}{N} \sum_{i=1}^N \int K(t) dt = \int K(t) dt \quad (\text{A.6})$$

Thus, as long as the integration of K is equal to 1, the integration of the estimated density function can be guaranteed as 1. The standard normal distribution can be used as kernel function, whose expression is:

$$K(t) = \frac{1}{\sqrt{2\pi}} e^{-\frac{t^2}{2}} \quad (\text{A.7})$$

Notice that the choice of h (also called bandwidth) in Eq.A.5 influence the goodness of KDE model. Here, Silverman's rule of thumb algorithm is used as bandwidth selector due to its universality and effectiveness:

$$h = 0.9 * \min(\hat{\sigma}, IQR/1.35) N^{-\frac{1}{5}} \quad (\text{A.8})$$

where $\hat{\sigma}$ is the standard deviation of samples and IQR is interquartile range (the difference between 75th and 25th percentiles).

Appendix B. Kullback-Leibler Divergence [31]

Since both experimental and simulation results in section 4.3 are distributions $(f_{We}(x), f_{De}(x), f_{WPGD}(x), f_{DPGD}(x))$, Kullback-Leibler Divergence (KLD) can be

used here to express difference between two continuous probability density distributions. KLD has its origins in the entropy of information theory, typically denoted as H . The definition of entropy for a probability distribution is:

$$H = - \int_x p(x) \log(p(x)) dx \quad (\text{B.1})$$

where $p(x)$ is the probability density function of any random x . With the help of entropy, information can be quantified, and the loss of information can be measured when the observed distribution is substituted with parameterized approximation. Similarly, rather than just having probability distribution $p(x)$, KLD adds in the approximating distribution $q(x)$ and takes logarithm operation:

$$D_{KL}(p(x), q(x)) = - \int_x p(x) \log(p(x) - q(x)) dx \quad (\text{B.2})$$

Essentially, KLD is the expectation of the log difference between the original (experimental) distribution with the approximating (simulated) distribution. A more common way to see KL divergence written is as follows:

$$D_{KL}(p(x), q(x)) = \int_x p(x) \log\left(\frac{q(x)}{p(x)}\right) dx \quad (\text{B.3})$$

References

- [1] V. Petrovic, J. V. H. Gonzalez, O. J. Ferrando, J. D. Gordillo, J. R. B. Puchades, L. P. Griñan, Additive layered manufacturing: sectors of industrial application shown through case studies, *International Journal of Production Research* 49 (4) (2011) 1061–1079.
- [2] C. Yan, L. Hao, A. Hussein, D. Raymont, Evaluations of cellular lattice structures manufactured using selective laser melting, *International Journal of Machine Tools & Manufacture* 62 (2012) 32–38.
- [3] N. Guo, M. C. Leu, Additive manufacturing: technology, applications and research needs, *Frontiers of mechanical engineering* 8 (3) (2013) 215–243.
- [4] R. Cunningham, S. P. Narra, C. Montgomery, J. Beuth, A. Rollett, Synchrotron-based x-ray microtomography characterization of the effect of processing variables on porosity formation in laser power-bed additive manufacturing of ti-6al-4v, *Jom* 69 (3) (2017) 479–484.
- [5] M. Tang, P. C. Pistorius, J. L. Beuth, Prediction of lack-of-fusion porosity for powder bed fusion, *Additive Manufacturing* 14 (2017) 39–48.
- [6] A. Yadollahi, N. Shamsaei, Additive manufacturing of fatigue resistant materials: Challenges and opportunities, *International Journal of Fatigue* 98 (2017) 14–31.

- [7] B. Whip, L. Sheridan, J. Gockel, The effect of primary processing parameters on surface roughness in laser powder bed additive manufacturing, *The International Journal of Advanced Manufacturing Technology* 103 (9) (2019) 4411–4422.
- [8] G. D. Goh, S. L. Sing, W. Y. Yeong, A review on machine learning in 3d printing: applications, potential, and challenges, *Artificial Intelligence Review* 54 (1) (2021) 63–94.
- [9] P. Witherell, S. Feng, T. W. Simpson, D. B. Saint John, P. Michaleris, Z.-K. Liu, L.-Q. Chen, R. Martukanitz, Toward metamodels for composable and reusable additive manufacturing process models, *Journal of Manufacturing Science and Engineering* 136 (6) (2014).
- [10] H. Yeung, Z. Yang, L. Yan, A meltpool prediction based scan strategy for powder bed fusion additive manufacturing, *Additive Manufacturing* 35 (2020) 101383.
- [11] C. Qiu, Z. Wang, A. S. Aladawi, M. A. Kindi, I. A. Hatmi, H. Chen, L. Chen, Influence of laser processing strategy and remelting on surface structure and porosity development during selective laser melting of a metallic material, *Metallurgical and Materials Transactions A* 50 (9) (2019) 4423–4434.
- [12] Z. Gan, K. Jones, Y. Lu, W. Liu, Benchmark study of melted track geometries in laser powder bed fusion of inconel 625, *Integrating Materials and Manufacturing Innovation* 10 (2) (2021) 177–195.
- [13] S. Ghosh, L. Ma, L. E. Levine, R. E. Ricker, M. R. Stoudt, J. C. Heigel, J. E. Guyer, Single-track melt-pool measurements and microstructures in inconel 625, *Jom* 70 (6) (2018) 1011–1016.
- [14] J. Smith, W. Xiong, J. Cao, W. K. Liu, Thermodynamically consistent microstructure prediction of additively manufactured materials, *Computational mechanics* 57 (3) (2016) 359–370.
- [15] W. Yan, Y. Lu, K. Jones, Z. Yang, J. Fox, P. Witherell, G. Wagner, W. K. Liu, Data-driven characterization of thermal models for powder-bed-fusion additive manufacturing, *Additive manufacturing* 36 (2020) 101503.
- [16] E. J. Schwalbach, M. G. Chapman, M. A. Groeber, Aflr additive manufacturing modeling series: Challenge 2, microscale process-to-structure data description, *Integrating Materials and Manufacturing Innovation* 10 (3) (2021) 319–337.
- [17] J. Zhao, M. Easton, M. Qian, M. Leary, M. Brandt, Effect of building direction on porosity and fatigue life of selective laser melted alsi12mg alloy, *Materials Science and Engineering: A* 729 (2018) 76–85.
- [18] H. Zhang, M. Xu, Z. Liu, C. Li, P. Kumar, Z. Liu, Y. Zhang, Microstructure, surface quality, residual stress, fatigue behavior and damage mechanisms of selective laser melted 304l stainless steel considering building direction, *Additive Manufacturing* 46 (2021) 102147.

- [19] Z. Hu, S. Mahadevan, Uncertainty quantification and management in additive manufacturing: current status, needs, and opportunities, *The International Journal of Advanced Manufacturing Technology* 93 (5) (2017) 2855–2874.
- [20] Y. Li, Y. Wang, R. Ma, P. Hao, Improved reliability-based design optimization of non-uniformly stiffened spherical dome, *Structural and Multidisciplinary Optimization* 60 (1) (2019) 375–392.
- [21] T. Moges, G. Ameta, P. Witherell, A review of model inaccuracy and parameter uncertainty in laser powder bed fusion models and simulations, *Journal of manufacturing science and engineering* 141 (4) (2019).
- [22] G. Strano, L. Hao, R. M. Everson, K. E. Evans, Surface roughness analysis, modelling and prediction in selective laser melting, *Journal of Materials Processing Technology* 213 (4) (2013) 589–597.
- [23] Surface Roughness Prediction in Additive Manufacturing Using Machine Learning, Vol. Volume 3: Manufacturing Equipment and Systems of International Manufacturing Science and Engineering Conference.
- [24] J. Ning, D. E. Sievers, H. Garmestani, S. Y. Liang, Analytical modeling of part porosity in metal additive manufacturing, *International Journal of Mechanical Sciences* 172 (2020) 105428.
- [25] Y. Lu, N. Blal, A. Gravouil, Adaptive sparse grid based HOPGD: Toward a nonintrusive strategy for constructing space-time welding computational vademecum, *International Journal for Numerical Methods in Engineering* 114 (13) (2018) 1438–1461.
- [26] Y. Lu, N. Blal, A. Gravouil, Datadriven hopgd based computational vademecum for welding parameter identification, *Computational mechanics* 64 (1) (2019) 47–62.
- [27] Z. Gan, Y. Lian, S. E. Lin, K. K. Jones, W. K. Liu, G. J. Wagner, Benchmark study of thermal behavior, surface topography, and dendritic microstructure in selective laser melting of inconel 625, *Integrating Materials and Manufacturing Innovation* 8 (2) (2019) 178–193.
- [28] J. Zhao, M. Easton, M. Qian, M. Leary, M. Brandt, Effect of building direction on porosity and fatigue life of selective laser melted alsi12mg alloy, *Materials Science and Engineering: A* 729 (2018) 76–85.
- [29] H. Qu, J. Li, F. Zhang, J. Bai, Anisotropic cellular structure and texture microstructure of 316l stainless steel fabricated by selective laser melting via rotation scanning strategy, *Materials and Design* 215 (2022) 110454.
- [30] R. A. Davis, K.-S. Lii, D. N. Politis, *Remarks on Some Nonparametric Estimates of a Density Function*, Springer New York, 2011, pp. 95–100.

- [31] S. Kullback, R. A. Leibler, On Information and Sufficiency, *The Annals of Mathematical Statistics* 22 (1) (1951) 79–86.
- [32] W. K. Hastings, Monte carlo sampling methods using markov chains and their applications, *Biometrika* 57 (1970) 97–109.
- [33] M. E. Cox, E. J. Schwalbach, B. J. Blaiszik, M. A. Groeber, Aifl additive manufacturing modeling challenge series: Overview, *Integrating Materials and Manufacturing Innovation* 10 (2021) 125 – 128.
- [34] Y. Lu, K. K. Jones, Z. Gan, W. K. Liu, Adaptive hyper reduction for additive manufacturing thermal fluid analysis, *Computer Methods in Applied Mechanics and Engineering* 372 (2020) 113312.
- [35] J. Ye, S. A. Khairallah, A. M. Rubenchik, M. F. Crumb, G. Guss, J. Belak, M. J. Matthews, Energy coupling mechanisms and scaling behavior associated with laser powder bed fusion additive manufacturing, *Advanced Engineering Materials* 21 (7) (2019).
- [36] R. Fabbro, M. Dal, P. Peyre, F. Coste, M. Schneider, V. Gunenthiram, Analysis and possible estimation of keyhole depths evolution, using laser operating parameters and material properties, *Journal of Laser Applications* 30 (3) (2018) 032410.
- [37] Capriccioli, P. Frosi, Fe procedure for welding processes simulation, 2009.
- [38] R. E. Pawel, R. K. Williams, Survey of physical property data for several alloys. [nitronic 33; copper c10400; copper c17510] 17 (6) (1985).
- [39] J. J. Valencia, P. N. Quested, *Thermophysical properties* (2013).
- [40] H. Yeung, B. Lane, A residual heat compensation based scan strategy for powder bed fusion additive manufacturing, *Manufacturing letters* 25 (2020) 56–59.
- [41] Y. Lu, N. Blal, A. Gravouil, Multi-parametric space-time computational vademecum for parametric studies: Application to real time welding simulations, *Finite Elements in Analysis and Design* 139 (2018) 62–72.
- [42] Y. Lu, N. Blal, A. Gravouil, Space-time pod based computational vademecums for parametric studies: application to thermo-mechanical problems, *Advanced Modeling and Simulation in Engineering Sciences* 5 (1) (2018) 1–27.
- [43] S. Saha, O. L. Kafka, Y. Lu, C. Yu, W. K. Liu, Microscale structure to property prediction for additively manufactured in625 through advanced material model parameter identification, *Integrating Materials and Manufacturing Innovation* 10 (2) (2021) 142–156.
- [44] E. P. DeGarmo, J. T. Black, R. A. Kohser, B. E. Klamecki, *Materials and process in manufacturing*, 1997.

- [45] I. Koutiri, E. Pessard, P. Peyre, O. Amlou, T. De Terris, Influence of slm process parameters on the surface finish, porosity rate and fatigue behavior of as-built inconel 625 parts, *Journal of Materials Processing Technology* 255 (2018) 536–546.
- [46] U. S. Bertoli, A. J. Wolfer, M. J. Matthews, J.-P. R. Delplanque, J. M. Schoenung, On the limitations of volumetric energy density as a design parameter for selective laser melting, *Materials & Design* 113 (2017) 331–340.